

# An imaging-plate detector for small-angle neutron scattering

Y. T. Cheng,<sup>a\*</sup> D. F. R. Mildner,<sup>b</sup> H. H. Chen-Mayer,<sup>b</sup> V. A. Sharov<sup>b†</sup> and C. J. Glinka<sup>b</sup><sup>a</sup>NeuTek, 13537 Scottish Autumn Lane, Darnestown, MD 20878, USA, and <sup>b</sup>National Institute of Standards & Technology, Gaithersburg, MD 20899, USA. Correspondence e-mail: neutekytc@aol.com

Small-angle neutron scattering (SANS) measurements have been performed on long-flight-path pinhole-collimation SANS instruments using, as a two-dimensional position-sensitive detector, both a neutron imaging plate, incorporating gadolinium, and a two-step transfer method, with dysprosium foil as the image transfer medium. The measurements are compared with corresponding data taken using conventional position-sensitive gas proportional counters on the SANS instruments in order to assess the viability of the imaging techniques. The imaging plates have pixel sizes of about two orders of magnitude smaller than those of the gas proportional counter. The reduced pixel size provides definite advantages over the gas counter in certain specific situations, namely when limited space necessitates a short sample-to-detector distance, when only small samples (comparable in size to the detector pixels) are available, or when used in conjunction with focusing beam optics.

© 2000 International Union of Crystallography  
Printed in Great Britain – all rights reserved

## 1. Introduction

Imaging plate (IP) technology enables a direct means of recording the distribution of intensity of radiation and has replaced conventional film in routine X-ray crystallography and studies involving the use of synchrotron radiation sources. The advantages of this technology include high spatial resolution, high sensitivity and a linear response to radiation dose over five orders of magnitude. Current commercial IP systems have a read-out spatial resolution ranging from 25 to 200  $\mu\text{m}$  and single plate sizes up to 350  $\times$  420 mm. The success of IPs as large-area  $\gamma$ /X-ray and charged-particle detectors has prompted a global effort to adapt the plates for neutron detection purposes. The development of this technology has allowed the design of a new generation of high resolution, compact and economic neutron detectors.

IPs typically consist of a flexible plastic sheet coated with a thin ( $\sim 10 \mu\text{m}$ ) photostimulable phosphor (e.g. BaFBr doped with  $\text{Eu}^{2+}$  ions). Ionizing radiation causes electrons to be trapped in defect sites; the density of defects is proportional to the received radiation. The trapped electrons are not released until the IP is stimulated under scanning by a fine helium–neon laser beam in the reader unit, causing the neighboring phosphors of the electrons to fluoresce. A photomultiplier tube detects the fluorescent light and records its intensity at the scanned positions, creating a digital image of the radiation field. After scanning, the IP can be erased quickly for reuse by exposure to intense light. The separation of IPs from their

laser reader unit means that multiple IPs can be used simultaneously for radiation monitoring, thus increasing the effective detector area.

Because the sensitivity of IPs to neutrons is low, neutron detection requires the use of a suitable converter to produce a more efficient form of ionizing radiation, such as energetic charged particles. Two methods of coupling a converter to an IP have been suggested and developed for neutron detectors for diffraction and scattering instruments (Bücherl *et al.*, 1993). The first is to place in front of the IP a foil with a high neutron absorption cross section (such as gadolinium) that emits prompt  $\gamma$ -rays or charged particles after neutron absorption (Wilkinson *et al.*, 1992). Higher spatial resolution and lower background can be obtained (Rausch *et al.*, 1992; Niimura *et al.*, 1994) by using the second method, namely that of incorporating the neutron converter material within the standard phosphor matrix of the IP. Measurements have been made using IPs mixed with gadolinium or lithium (Niimura *et al.*, 1994, 1997; Cipriani, Castagna, Lehmann & Wilkinson, 1995; Cipriani, Castagna, Wilkinson *et al.*, 1995; Karasawa *et al.*, 1995; Thoms *et al.*, 1997; Takahashi *et al.*, 1996). The difficulty with both methods is that the IP is inherently sensitive to non-neutron background radiation, which compromises the signal-to-noise ratio of the measurement. Additional problems associated with using neutron IPs include image blooming effects (when signals near saturation cause bleeding into neighboring pixels) and residual images burned-in from overexposure to intense neutron beams. Nevertheless, Niimura *et al.* (1997) have successfully refined the positions of hydrogen atoms in a protein with bound water

<sup>†</sup> Present address: The Institute for Genomic Research, Rockville, MD 20850, USA.

molecules using Laue diffractometry with a neutron IP, despite the high background under the diffraction peaks from neutron incoherent scattering from the sample.

These difficulties can be avoided by applying a two-step transfer method in which the standard IP is used off-line. Instead of irradiating the IP, a foil with a high absorption cross section that emits delayed  $\gamma$ -rays or charged particles after neutron absorption is placed in the neutron field. The foil acts as a detector that collects and retains the intensity distribution information of the neutron field through the activation process. This retained information is subsequently retrieved by autoradiography, exposing the foil off-line to a standard IP or other radiation-imaging device. This means that only the metal foil is exposed to neutrons and activated, eliminating interference from background  $\gamma$  radiation.

The resultant radioactivity pattern in the foil therefore mirrors the neutron field distribution. After a predetermined activation time, the foil is taken out of the neutron field and placed in close contact with a radiation-imaging device, such as an IP, to create the excitation process in the plate. The IP is then read and the radiation information in the foil is converted to a digital image. Each pixel value is directly proportional to the localized neutron field intensity and a calibration procedure can be used to obtain the absolute neutron yield distribution. This two-step transfer approach completely eliminates the interference from non-neutron radiation. Hence, it reduces shielding requirements and offers the flexibility of tailoring the type, shape and size of foils, neutron activation time and IP exposure time to specific experimental conditions. For instance, the duration of the exposure time of the foil to an IP after activation can be used to shift the dynamic range of this measurement technique.

## 2. Small-angle neutron scattering

We have conducted small-angle neutron scattering (SANS) measurements to assess the performance of using IPs as an inexpensive two-dimensional detector. The approach includes both techniques for neutron detection: the activation of a dysprosium foil followed by its exposure to an IP (which we call the transfer method) and the use of a gadolinium-loaded neutron IP. The idea of using IPs as a large-area neutron detector for SANS measurements has been tested before by Né *et al.* (1993). They used a variation of the first method of conversion, *i.e.* in-beam conversion. Gadolinium powder was dispersed in paint and uniformly sprayed on a thin aluminium plate to give a conversion efficiency of about 50%. Né *et al.* found the aforementioned difficulties with this technique, that is, the activation of the IP itself by neutrons and the sensitivity to background  $\gamma$  radiation.

We also compare both techniques to the conventional method of employing a standard gas proportional counter as a two-dimensional detector for SANS. However, we note that it is important to consider the resolution of the measurement when making comparisons between different methods of recording data for small-angle scattering, lest misleading conclusions be made. Details of the evaluation of the SANS

resolution are given in Appendix A, together with the geometric factors for comparison of the fluence on the sample and the count rate in the detector.

Standard SANS instruments use high-efficiency (>70%) gas proportional counters as two-dimensional position-sensitive detectors. Generally they have pixel dimensions of 5 or 10 mm. This rather large pixel size is comparable with the lateral dimensions of neutron beams, which are usually required to be large because of the inherent weakness of neutron sources. Neutron beams with these lateral dimensions require long flight paths, of length  $\sim 10$  m or more, to achieve the necessary resolution at low scattering angles. The sample-to-detector distance, the neutron wavelength and the overall size of the detector determine the range of scattering vectors available on the instrument. The use of an IP as the two-dimensional detector reduces the pixel size to 0.1 mm or less. This means that the solid angle subtended by a detector pixel at the sample is greatly diminished and becomes negligible compared with the other contributions to the resolution. The reduction in the pixel size by two orders of magnitude implies that good angular resolution can be achieved with a much shorter secondary flight path, provided that the sample aperture can also be reduced proportionally, as required by the optimization criteria discussed in Appendix A.

## 3. Measurements

Measurements using the two-step transfer method of foil activation followed by subsequent exposure to the IP have been performed on the 30 m SANS spectrometer (Glinka *et al.*, 1998) on the NG-7 beamline at the National Center for Neutron Research. A dysprosium (Dy) foil of thickness 0.125 mm and a Fuji standard IP were used for the two-step process (Dy/IP) measurements. Apart from a short-lived metastable isotope ( $^{165m}\text{Dy}$ , half life 1.25 min), Dy is an almost pure  $\beta$  emitter upon activation ( $^{165}\text{Dy}$ , half life 2.35 h). For these measurements, the sample was placed at the exit of the incident flight path, from which all beam guides had been removed, so that the source-to-sample distance was 16.0 m. A Dy foil was placed inside an evacuated chamber, normally used for sample installation, so that the sample-to-detector distance,  $L_2$ , was 0.9 m, an order of magnitude smaller than for conventional SANS instruments. An extension tube was placed between the sample and chamber, so that the air gap after the sample was less than 100 mm. There was a time delay of approximately 20 min between the completion of the activation (usually for 2 h) of the Dy foil in the neutron beam and the exposure of the foil to the IP (also usually for 2 h), followed by a scanner read-out at 100  $\mu\text{m}$  resolution.

Measurements using the neutron-sensitive IP as the detector were performed at a wavelength,  $\lambda$ , of 0.5 nm on the 8 m SANS instrument (Glinka *et al.*, 1986), which views the cold source on beamline NG-1. The images were recorded with a gadolinium-loaded neutron IP (NIP), from Fuji Photo Film, placed at a distance of 0.75 m beyond the sample, with a 100  $\mu\text{m}$  pixel read-out size. The IP has a BaFBr phosphor layer, 120  $\mu\text{m}$  thick, with a  $\text{Gd}_2\text{O}_3$  converter, in a Ba/Gd

molecular mixture of 1:1 and with a density of  $3.5 \text{ g cm}^{-3}$ , on a flexible plastic (polyethylene terephthalate) backing (Nimura *et al.*, 1994). The neutron IP technique was also used with the 30 m SANS instrument. The measurements have been compared with those recorded using the conventional detector and both instruments.

Test measurements were performed on three different samples, as follows. (i) A shear-oriented layered block copolymer, with equatorial peaks at  $Q = 0.194 \text{ nm}^{-1}$ , was supplied by Frank Bates, University of Minnesota. (ii) A Bioran CPG (controlled pore glass) was obtained from Schott Geräte Gmgh of Hofhelm/Taunus, Germany. This is a special glass used in separation science. Its porous silicon dioxide structure ( $\text{SiO}_2 > 96\%$ ) is sponge-like with high porosity ( $\sim 70\%$ ) and a material bulk density of  $0.4 \text{ g ml}^{-1}$ . The pores are largely uniform in size. It exhibits a characteristically sharp distribution that is significantly narrower than for silica gels. Bioran G100 has pores of dimension 100 nm and an azimuthally symmetric scattering peak at  $0.0403 \text{ nm}^{-1}$ . (iii) A powder sample of silver behenate,  $(\text{CH}_3)(\text{CH}_2)_{20}\text{COOAg}$ , a long-chain silver carboxylate, was obtained from Eastman Kodak Co. This compound has a long period spacing,  $d(00l)$ , of 5.8380 (3) nm, with a corresponding azimuthally symmetric peak at a scattering vector value  $Q = 1.076 \text{ nm}^{-1}$  (Huang *et al.*, 1993). Its use as a SANS wavelength calibration standard (Gilles *et al.*, 1998) has been suggested.

## 4. Results

### 4.1. Layered block copolymer

The first sample studied was the block copolymer (at wavelength  $\lambda = 0.6 \text{ nm}$ , with wavelength spread  $\Delta\lambda/\lambda = 11\%$ ), exhibiting two equatorial peaks at  $Q_p = 0.194 \text{ nm}^{-1}$ , from

which the lamellar spacing,  $d = 2\pi/Q_p$ , of the ordered phase of the diblock copolymer can be determined.

**4.1.1. Transfer method (Dy/IP).**  $L_1$  was set at 16 m. A Dy foil was placed behind a semitransparent beam-stop inside the evacuated chamber with  $L_2 = 0.9 \text{ m}$ . The source aperture  $R_1$  was 19 mm so that the optimum sample radius  $R_2$  should be 1 mm [see equation (5) in Appendix A]. In practice, we chose  $R_2 = 1.2 \text{ mm}$ . This gives  $R_{\text{min}} = 2.34 \text{ mm}$  and a minimum scattering vector value  $Q_{\text{min}} = 0.028 \text{ nm}^{-1}$ . The Dy foil was exposed for about 35 min. The foil was then placed in contact with an IP for 2 h. The image (magnified by a factor of two) shown in Fig. 1(a) indicates scattering peaks at a scattering vector value of  $0.198 \text{ nm}^{-1}$ . The measured intensity shows that the signal in the vicinity of the peak is a factor of 275 greater than the background. Table 1 gives the various contributions to the resolution, indicating that the detector pixel contribution is negligible and the wavelength contribution at this scattering vector is comparable with the other terms.

**4.1.2. Neutron imaging plate (NIP).** This measurement was repeated with all parameters unchanged but with a Gd-loaded NIP in place of the Dy foil as the neutron detector. A  $^6\text{Li}$ -poly beam-stop of radius 7.5 mm (equivalent to  $Q = 0.087 \text{ nm}^{-1}$ ), necessary to prevent saturation of the NIP by the direct beam, was suspended on wires in front of the IP. (A blooming effect has been observed when an NIP is near saturation.) Fig. 1(b) shows the SANS image of the block copolymer recorded with the NIP. Comparison of the two images in Fig. 1 clearly indicates the cleaner data for the foil transfer process relative to the Gd-loaded IP method for the block copolymer. Fig. 2 places this comparison on a quantitative scale by showing a scan through the images of the SANS profiles of the block copolymer. The NIP profile shows an intensity three times greater than for the transfer method for these measurements, and with no direct beam. However, the signal-to-noise ratio

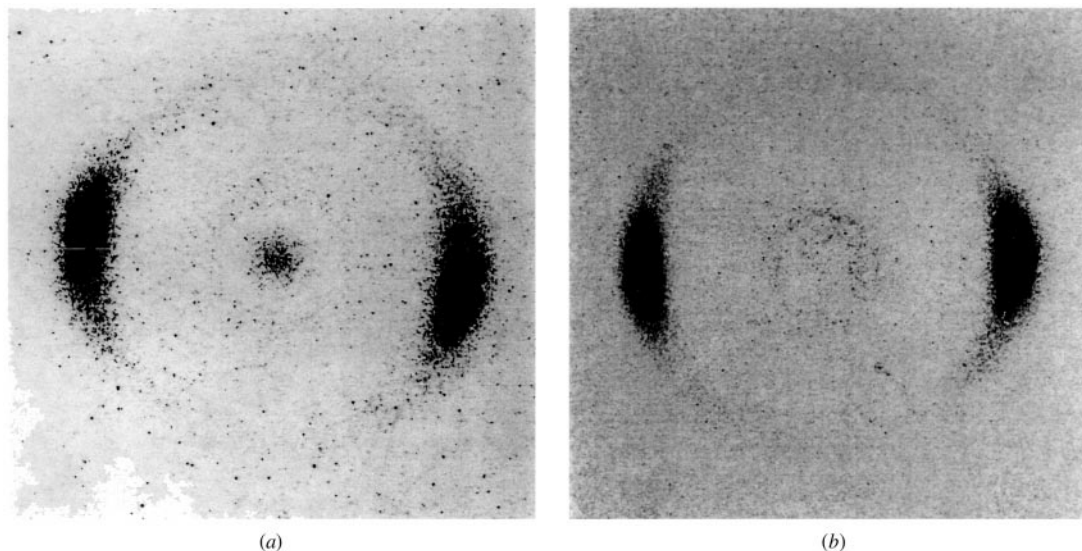


**Figure 1**

The SANS pattern of a layered block copolymer imaged (a) by the Dy-foil transfer method and (b) by a Gd-loaded NIP. Both sets of data were taken at the NG-7 instrument using 0.6 nm neutrons.

**Table 1**

Contributions to the resolution [equation (4)] ( $\text{nm}^{-1}$ ) at  $Q_p = 0.194 \text{ nm}^{-1}$  for the layered block copolymer on the NG-7 instrument.

Both measurements were taken at  $\lambda = 0.6 \text{ nm}$  ( $\Delta\lambda/\lambda = 11\%$ ).

Term	Dy/IP and NIP	Gas detector
$(1/2)k(R_1/L_1)$	0.0062	0.0062
$(1/2)kR_2(L_1^{-1} + L_2^{-1})$	0.0074	0.0013
$[1/(12^{1/2})]k(\Delta R/L_2)$	0.0003	0.0044
$[1/(6^{1/2})]Q(\Delta\lambda/\lambda)$	0.0087	0.0087
$\sigma_Q$	0.0130	0.0116
$Q_{\min}$	0.0284	0.0302

around the peak for the NIP is about 15, which is an order of magnitude worse than for the transfer method.

**4.1.3. Gas proportional detector.** The position-sensitive gas proportional detector of the NG-7 SANS instrument has also been used to measure the same scattering pattern using the same incident flight path, that is, with the same fluence on the sample, but with  $L_2 = 6.9 \text{ m}$ . This gives  $R_{\min} = 9.9 \text{ mm}$  and  $Q_{\min} = 0.030 \text{ nm}^{-1}$ . Fig. 3 shows an image of the scattering pattern with a scattering peak at  $Q_p = 0.194 \text{ nm}^{-1}$  after 8 min counting time. A profile generated by scanning through the pattern is shown in Fig. 4. The signal-to-noise ratio is about 170, which compares favorably with that of the NIP but is lower than found with the Dy/IP transfer method.

With the proportional counter one can use a larger sample aperture and a longer secondary flight path to optimize the signal. For example,  $R_2$  can be increased to 5.7 mm by the optimization of equation (5), giving  $Q_{\min} = 0.040 \text{ nm}^{-1}$ . This results in an increased count rate by a factor greater than 22, while the resolution is scarcely increased because the wavelength term dominates in equation (4) (see Appendix A). In fact, this term results in the overall resolution being about the same for all three measurements of this peak.

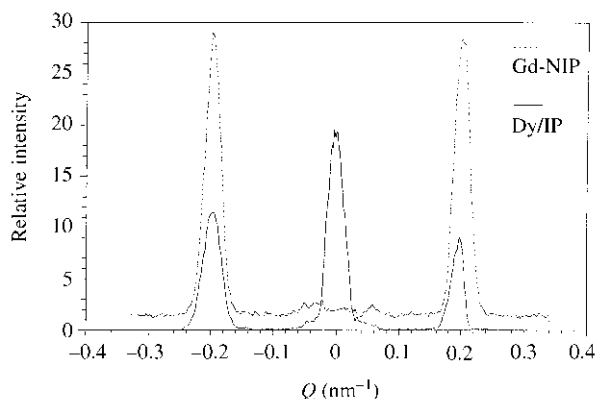


**Figure 2**

Profiles of the SANS data of a layered block copolymer measured (a) by the Dy-foil transfer method (with a semitransparent beam-stop) and (b) by a Gd-loaded NIP (with a  $^6\text{Li}$ -poly beam-stop) at the NG-7 instrument using 0.6 nm neutrons, showing the equatorial peaks at a scattering vector value  $Q_p = 0.194 \text{ nm}^{-1}$  and the superior signal-to-noise ratio of the transfer method.

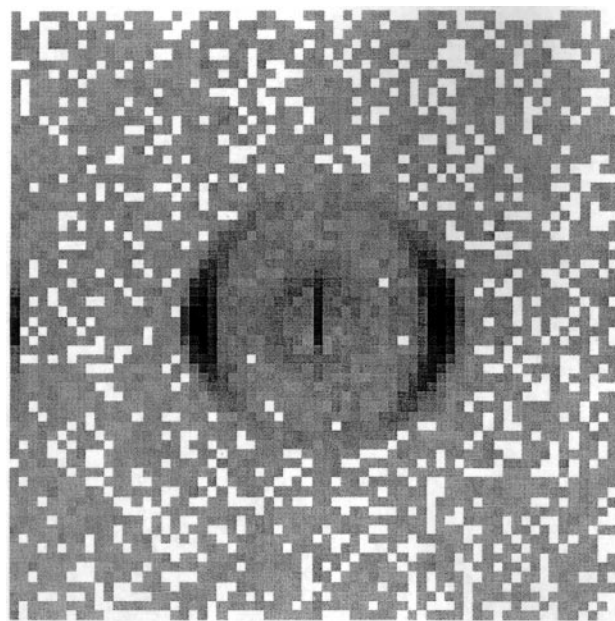


**Figure 3**

An image of the SANS pattern of a layered block copolymer, showing the equatorial peaks at a scattering vector value  $Q = 0.194 \text{ nm}^{-1}$ .

#### 4.2. Bioran CPG

The second measurement was an attempt to resolve the scattering peak from Bioran CPG with 100 nm pore size.

**4.2.1. Transfer method.** The wavelength selected was 0.6 nm (with  $\Delta\lambda/\lambda = 22\%$ ). The sample was placed at the exit of the incident flight path. A Dy foil was placed, without a beam-stop, inside the evacuated chamber at a distance  $L_2 = 0.9 \text{ m}$ . After exposure for 2 h, the Dy foil was placed in contact with an IP for 2 h. With the source aperture  $R_1 = 11 \text{ mm}$ , the sample radius  $R_2$  should be 0.6 mm; however, in practice,  $R_2$  was chosen to be 0.25 mm (corresponding to  $R_{\min} = 0.88 \text{ mm}$  and  $Q_{\min} = 0.011 \text{ nm}^{-1}$ ) to ensure that the azimuthally symmetric scattering peak was well resolved. The image shown in Fig. 5(a) is a SANS pattern for the Bioran sample, illustrating the excellent spatial resolution of the Dy-foil transfer method.

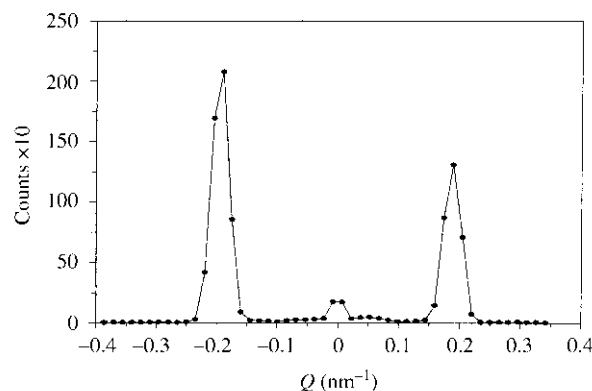


**Figure 4**

The profile of the SANS data (Fig. 3) of a layered block copolymer measured on the NG-7 instrument using 0.6 nm neutrons and a gas proportional detector.

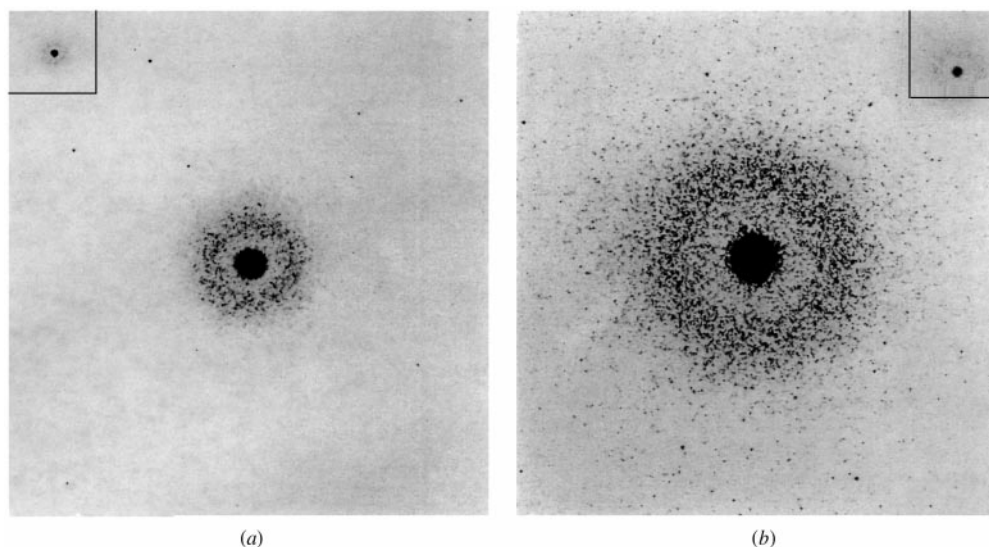


**Figure 5** Images of the SANS patterns from a Bioran G100 sample imaged by the transfer method on the NG-7 instrument using neutrons of wavelength (a) 0.6 nm and (b) 1.2 nm. The insets are SANS images of 70% actual size.

Fig. 6 shows a radial average of this image with step sizes of  $\Delta R = 0.1$  mm (equivalent to  $\Delta Q = 0.0012$  nm<sup>-1</sup>). The peak appears at a scattering vector value of  $Q_p = 0.0402$  nm<sup>-1</sup>, where the resolution is  $\sigma_Q = 0.00535$  nm<sup>-1</sup>. The contribution to the resolution from the pixel size of the IP is negligible (see Table 2) and the contribution from the sample is also small. The source contribution and the wavelength contribution at this particular magnitude of scattering vector are comparable and dominant.

**4.2.2. Gas proportional detector.** A measurement was also conducted on the NG-7 SANS instrument in its normal configuration, using the conventional gas counter and  $\lambda = 1.2$  nm (with  $\Delta\lambda/\lambda = 11\%$ ), corresponding to  $R_{\min} = 19.4$  mm and  $Q_{\min} = 0.013$  nm<sup>-1</sup>. Fig. 7 shows the SANS profile after 5 min, indicating the peak at a scattering vector value  $Q_p$  of  $0.0405$  nm<sup>-1</sup>. This corresponds to a pore size of  $2\pi/(Q_p)p = 104$  nm, where  $p = 0.67$  is the porosity. The detector has a pixel size of  $10 \times 10$  mm, so that a detector spatial resolution of 10 mm corresponds to a data step size of  $\Delta Q = 0.00436$  nm<sup>-1</sup>. The resolution at the peak in the data is  $\sigma_Q = 0.0038$  nm<sup>-1</sup>. The detector spatial resolution provides the smallest contribution to the  $Q$  resolution. The sample contribution is approximately twice that of both the source contribution and the wavelength contribution at this particular magnitude of scattering vector (see Table 2).

**4.2.3. Transfer method at  $\lambda = 1.2$  nm.** To provide a more direct comparison, measurements according to the transfer method were repeated using neutrons of  $\lambda = 1.2$  nm (with  $\Delta\lambda/\lambda = 11\%$ ), with the other parameters unchanged. A Dy foil was again exposed to neutrons for 2 h, despite a reduction of  $\sim 16$  in neutron beam intensity at this longer wavelength. Fig. 5(b) shows a SANS image, recorded by the Dy/IP transfer method. Fig. 6 shows a radial average of this image with steps sizes of  $\Delta R = 0.1$  mm (equivalent to  $\Delta Q = 0.00058$  nm<sup>-1</sup>). The scattering peak is well resolved, though there is some peak

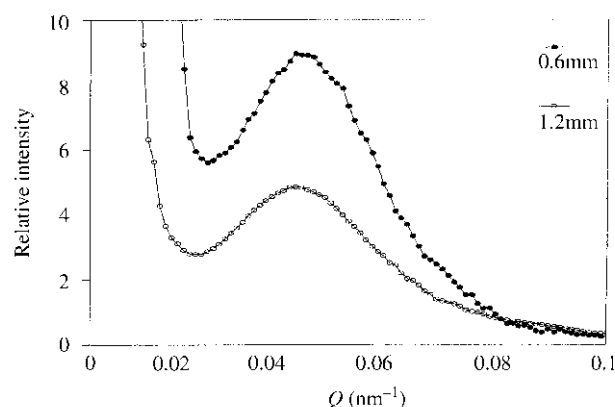


**Figure 6** The radial average of the SANS data (Fig. 5) of a Bioran G100 sample measured by the transfer method on the NG-7 instrument using both 0.6 nm and 1.2 nm neutrons, showing the tail of the incident beam.

**Table 2** Contributions to the resolution [equation (4)] (nm<sup>-1</sup>) at  $Q_p = 0.0405$  nm<sup>-1</sup> for the Bioran G100 sample on the NG-7 instrument.

The Dy/IP measurements were taken at both  $\lambda = 0.6$  nm ( $\Delta\lambda/\lambda = 22\%$ ) and  $\lambda = 1.2$  nm ( $\Delta\lambda/\lambda = 11\%$ ), whereas the gas-detector measurement was taken only at  $\lambda = 1.2$  nm ( $\Delta\lambda/\lambda = 11\%$ ).

Term	Dy/IP ( $\lambda = 0.6$ nm)	Dy/IP ( $\lambda = 1.2$ nm)	Gas detector ( $\lambda = 1.2$ nm)
$(1/2)k(R_1/L_1)$	0.0036	0.0018	0.0018
$(1/2)kR_2(L_1^{-1} + L_2^{-1})$	0.0015	0.0008	0.0025
$[1/(12^{1/2})]k(\Delta R/L_2)$	0.0003	0.0002	0.0013
$[1/(6^{1/2})]Q(\Delta\lambda/\lambda)$	0.0036	0.0018	0.0018
$\sigma_Q$	0.0054	0.0027	0.0038
$Q_{\min}$	0.0114	0.0057	0.0129

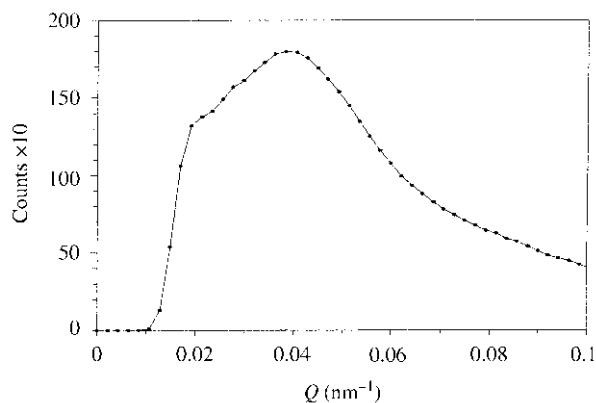


**Figure 7**  
The radial average of the SANS data of a Bioran G100 sample measured by the gas proportional counter on the NG-7 instrument using 1.2 nm neutrons. The data are cut off by the beam-stop at the lowest scattering vectors.

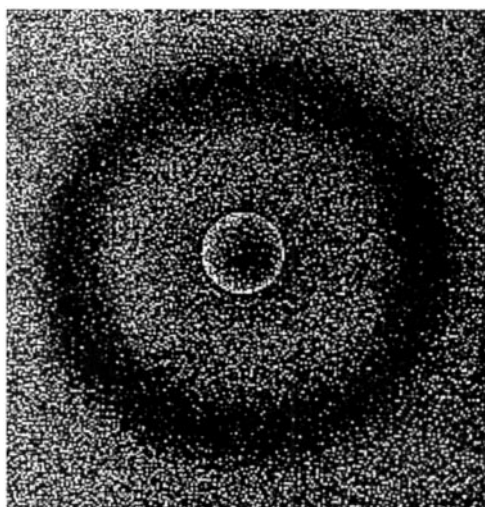


**Figure 8**  
The image of the SANS pattern from a silver behenate sample measured by a Gd-loaded NIP at the NG-1 instrument using 0.5 nm neutrons.

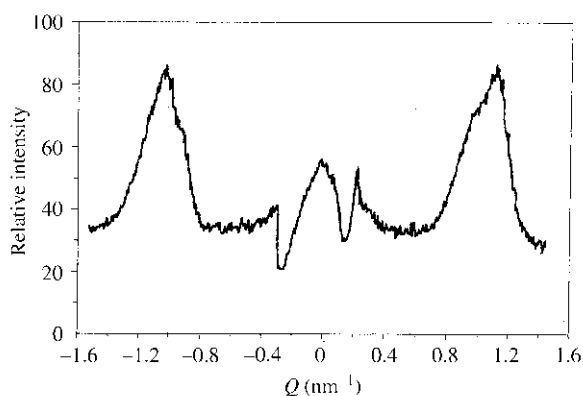


**Figure 9**  
The profile of the SANS data (Fig. 8) of a silver behenate sample measured by a Gd-loaded NIP at the NG-1 instrument using 0.5 nm neutrons.

broadening with the use of longer wavelength neutrons caused by multiple scattering.

#### 4.3. Silver behenate

The third sample was silver behenate with a diffraction peak at  $Q = 1.076 \text{ nm}^{-1}$ , though unlike in the other measurements, the large incoherent scattering from the hydrogenous sample dominated the background. The sample was measured on another instrument, the NG-1 8 m SANS device, using  $\lambda = 0.5 \text{ nm}$  ( $\Delta\lambda/\lambda = 25\%$ ) with a sample transmission of 0.74, to compare the performances of the Gd-loaded NIP and a two-dimensional gas proportional counter with a spatial resolution (full width at half-maximum, FWHM) of  $\sim 15\text{--}20 \text{ mm}$ .

**4.3.1. Neutron imaging plate.** The NIP was placed at a distance of 0.75 m downstream from the sample position. The conditions of the measurement define  $R_{\min} = 6.63 \text{ mm}$ , or  $Q_{\min} = 0.113 \text{ nm}^{-1}$ . Unlike the foil transfer method, measurement with the NIP requires the use of a beam-stop (without it the SANS signal would be buried within the blurred image of the transmitted beam). This suggests that a considerable fraction of the neutron beam causes ionizing radiation extending over hundreds of pixels within the NIP. Consequently, the measurement was conducted with a  $^6\text{Li}$ -poly beam-stop of radius 14.3 mm (equivalent to  $Q_{\min} = 0.240 \text{ nm}^{-1}$ ) suspended on wires in front of the NIP. This enables the diffraction ring to be observed well separated from the beam-stop. Fig. 8 shows the diffraction image on the NIP after a 14 h exposure, indicating the peak at  $Q = 1.083 \text{ nm}^{-1}$ . The resolution at this scattering vector is  $\sigma_Q = 0.12 \text{ nm}^{-1}$  and is dominated by the wavelength term in equation (4) as is shown in Table 3. Fig. 9 shows a profile through these data, indicating that the peak has width  $\Delta Q = 0.325 \text{ nm}^{-1}$ .

**4.3.2. Gas proportional detector.** Small-angle scattering was also performed on this same sample with the instrument in its normal configuration, using the standard gas proportional counter, corresponding to  $R_{\min} = 21.6 \text{ mm}$ , or  $Q_{\min} = 0.110 \text{ nm}^{-1}$ . Fig. 10 shows the circularly averaged data with a peak at  $Q_p = 1.065 \text{ nm}^{-1}$ , with width  $\Delta Q = 0.31 \text{ nm}^{-1}$ . The resolution is  $\sigma_Q = 0.113 \text{ nm}^{-1}$  and is again dominated by the wavelength term (see Table 3).

Comparison of Figs. 9 and 10 shows that the performances of the two detection methods are approximately equal, with both the peak resolutions and the signal-to-noise ratios of the two profiles being comparable. However, this arises from the strong incoherent scattering which dominates the scattering away from the peak in this case.

#### 4.4. Count-rate comparisons

In making comparisons among different methods of data collection, care must be taken to compare like with like, lest inappropriate conclusions be drawn. With the small pixel sizes that are available with the IP technique, an appropriate detector element size suggested by the optimization equation (5), with  $\Delta R = (3/2)^{1/2}(L_2/L_1)R_1$ , can be chosen by summing together the necessary number of pixels. This value of the detector element is used in Table 4, which summarizes the

**Table 3**

Contributions to the resolution [equation (4)] ( $\text{nm}^{-1}$ ) at  $Q_p = 1.065 \text{ nm}^{-1}$  for the silver behenate sample on the NG-1 instrument.

Both measurements were taken at  $\lambda = 0.5 \text{ nm}$  ( $\Delta\lambda/\lambda = 25\%$ ).

Term	NIP	Gas detector
$(1/2)k(R_1/L_1)$	0.024	0.018
$(1/2)kR_2(L_1^{-1} + L_2^{-1})$	0.031	0.020
$[1/(12^{1/2})]k(\Delta R/L_2)$	0.001	0.015
$[1/(6^{1/2})]Q(\Delta\lambda/\lambda)$	0.109	0.109
$\sigma_Q$	0.116	0.113
$Q_{\min}$	0.113	0.127

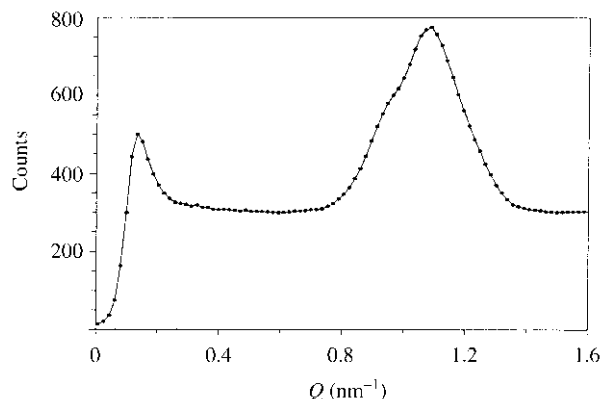


**Figure 10**

The radial average of the SANS data from a silver behenate sample measured by the gas proportional counter on the NG-1 instrument using 0.5 nm neutrons.

results of the three measurements together with modifications of experimental conditions in an attempt to make the measurements more comparable. Also shown for comparison are geometric ratios indicating the relative fluence on the sample, which is proportional to  $(R_1R_2/L_1)^2$ , the count rate measured at the detector, which is proportional to  $[(R_1R_2)/$

$(L_1L_2)]^2$ , and the count rate per detector element, which is proportional to  $[(R_1R_2\Delta R)/(L_1L_2)]^2$ . It is this last quantity, the proportionality constant, that relates the measured intensity to the scattering cross section and hence is the most relevant measure of performance. Note that optimized values of geometric parameters have not been strictly followed in all of the above measurements.

The geometries for the block-copolymer measurements with the IP method and with the gas detector are exactly the same, so that the count rates are similar. However, in cases where there is no restriction on the sample size, the conventional SANS method can obtain greater fluence on the sample and a greater count rate per pixel by increasing the sample area. The geometries for the measurements of the Bioran sample are quite different. Even at the same wavelength, the conventional method has a greater count rate per pixel by a factor of over 600, approximately the same factor by which the sample areas differ. For the silver behenate sample on the spectrometer of shorter length, the count rates per pixel are comparable. However, if the full source size is used for the gas detector measurement with a similar increase in sample size, the count rate per pixel is increased approximately by a factor of five.

## 5. Discussion

The requirements for a metal foil as a neutron-to-charged-particle converter suitable for use in conjunction with a standard IP are that it has a high neutron absorption cross section, a simple decay scheme and a reasonable half life. Dysprosium has been found to be the best candidate; it is an almost pure  $\beta$  emitter upon activation, though it is only useful for up to about 8 h of irradiation. However, the foil should not be re-used until after a decay of a couple of days (20 half-lives or a factor of  $10^6$ ). A discussion regarding dysprosium and

**Table 4**

Parameters for all experimental conditions.

	Block copolymer NG-7 instrument			Bioran G100 NG-7 instrument			Silver behenate NG-1 instrument		
	Dy/IP NIP	Gas detector		Dy/IP		Gas detector	NIP	Gas detector	
		Smaller $R_2$	Larger $R_2$	$\lambda = 0.6 \text{ nm}$	$\lambda = 1.2 \text{ nm}$			Smaller $R_1$	Larger $R_1$
Incident path $L_1$ (m)	16	16	16	16	16	16	4.5	4.5	4.5
Scattered path $L_2$ (m)	0.9	6.9	6.9	0.9	0.9	12	0.75	3.6	3.6
Source size $R_1$ (mm)	19	19	19	11	11	11	17.5	12.7	17.5
Sample size $R_2$ (mm)	1.2	1.2	5.7	0.25	0.25	6.5	3.18	6.35	7.78
Detector element $\Delta R$ (mm)†	1.31	10	10	0.76	0.76	10	3.57	15	17
Wavelength $\lambda$ (nm)	0.6	0.6	0.6	0.6	0.12	0.12	0.5	0.5	0.5
$\lambda$ resolution $\Delta\lambda$	0.11	0.11	0.11	0.22	0.11	0.11	0.25	0.25	0.25
$Q_{\min}$ ( $\text{nm}^{-1}$ )†	0.042	0.030	0.040	0.019	0.010	0.013	0.171	0.127	0.158
$\sigma_Q$ ( $\text{nm}^{-1}$ )†	0.014	0.012	0.013	0.0059	0.0029	0.0038	0.117	0.113	0.116
Fluence on sample, $(R_1R_2/L_1)^2 \times 10^{12}$	2.03	2.03	46.2	0.030	0.030	20.0	153	321	915
Count rate at detector, $[(R_1R_2)/(L_1L_2)]^2 \times 10^{12}$	2.51	0.043	0.971	0.037	0.037	0.139	272	24.8	70.6
Count rate per detector element, $[(R_1R_2\Delta R)/(L_1L_2)]^2 \times 10^{18}$	4.30	4.30	97.8	0.021	0.021	14.15	3465	5576	20765

† The appropriate detector element size is determined from the optimization equation (5),  $\Delta R = (3/2)^{1/2}(L_2/L_1)R_1$ , so that a large number of pixels are summed together for the IP technique. In this table, the values of the scattering vector resolution  $\sigma_Q$  and  $Q_{\min}$  take into account this larger  $\Delta R$ .

other possible foils is given elsewhere (Cheng & Mildner, 2000). For the measurements reported here, we estimate that the uncertainty is less than 1% (one standard deviation), requiring about  $5 \times 10^4$  neutrons  $\text{cm}^{-2}$ .

Though the one-step method is certainly more convenient, there are difficulties associated with the neutron-sensitive IP. There may be residual background from radioactivity from activated nuclei caused by the previous measurements. In addition, the neutron IP requires the use of a beam-stop in front of the IP to prevent blooming effects. The neutron-sensitive materials in a neutron IP emit  $\gamma$ /X-rays as well as charged particles when the neutron IP is exposed to a neutron field. This  $\gamma$ /X-ray emission adds background to the measurement and is the primary cause of some of the blooming effects observed when the IP is near saturation. Moreover, tracks from charged particles may spread out over many pixels. For example, a 5.5 MeV  $\alpha$  particle from  $^{238}\text{Pu}$  appears to affect about 10–15 pixels (pixel size 100  $\mu\text{m}$ ) (Cheng *et al.*, 1996), whereas  $\beta$  particles affect only about 1–3 pixels.

The Gd-loaded neutron IP is efficient in converting neutrons to measurable signals, and its neutron sensitivity and signal-to-noise are comparable to those of the standard gas counter. Though the transfer method is not as efficient and involves an additional step, its inherent insensitivity to radiation other than neutrons improves the signal-to-noise ratio and reduces the experimental  $\gamma$ -shielding requirement. One possibility for improving the neutron detection efficiency of the method is the use of multiple thin Dy foils instead of one relatively thick foil to capture the scattered neutrons, followed by the transfer of the neutron information by exposing each foil individually to separate IPs. This increases the neutron absorption but avoids the problem of  $\beta$  self-absorption in a thick foil. While the NIP can be read once only, the dynamic range of the two-step process can be extended by adjusting the exposure times and the sensitivity of the reader. For example, one can use a short exposure to record very high intensity signals and then use a longer exposure to record the weaker signals. However, perhaps the greatest limitation is that the technique is not on-line with live time data collection. It is an imaging detector that with small samples may be faster on an absolute time scale than traditional detectors for similar statistics.

## 6. Conclusions

We have shown that it is possible to perform small-angle neutron scattering measurements using either a neutron IP or a metal foil with a high neutron absorption cross section as the position-sensitive detector. A Dy foil is used in conjunction with a standard IP in a two-step transfer method to record the scattering signal. Both detection methods yield a scattering vector resolution comparable to that of the conventional two-dimensional gas proportional counter. Though the counter appears to be about 1.5 times more efficient than the transfer method, the inherent insensitivity of the transfer approach to non-neutron radiation interferences enables it to discriminate

against  $\gamma$  background even better than gas counters, which, under certain conditions, results in a superior signal-to-noise ratio. This allows more detail in the scattering pattern to be discerned. This insensitivity also means that the transfer method requires only minimum  $\gamma$  shielding.

IPs have pixel sizes that are about two orders of magnitude smaller than those of conventional two-dimensional gas detectors. This high spatial resolution is only useful when the sample area is of necessity very small, or when beam-focusing techniques become practical (Choi *et al.*, 2000). The small sample size is compensated by the shorter secondary flight path that can be used with IPs. The considerable reduction in the secondary flight path and the replacement of the large-area position-sensitive detector can enable SANS instruments to be operated in experimental environments where space is limited.

The transfer method also has advantages as a neutron detector over the Gd- or Li-loaded neutron IPs. Unlike the transfer method, the neutron IP detects neutrons directly and is about as efficient as the gas counters. However, the neutron IP is sensitive to  $\gamma$ /X-ray background present in most neutron environments. Unlike wide-angle diffraction, small-angle scattering requires that the detector be protected from the incident beam by a beam-stop; otherwise, the neutron IP suffers from a large beam spill-over which is detrimental to the measurement. This is not a problem with the transfer method. Other potential problems associated with the neutron IP include the depletion of the loaded neutron-sensitive material and burned-in residual radioactivity from repeated use.

## APPENDIX A

### Small-angle neutron scattering resolution

The scattered intensity is measured as a function of the scattering angle  $\theta$ , or the magnitude of the scattering vector  $Q = k\theta$ , where the incident wavevector value  $k = (2\pi)/\lambda$  corresponds to the wavelength  $\lambda$ . In practice, the measurement is recorded on a two-dimensional position-sensitive detector as a function of the radial distance  $R$  from the beam axis. Now the scattering vector is defined by

$$Q = k\theta = (2\pi/\lambda)(R/L_2), \quad (1)$$

where  $L_2$  is the distance from the sample to the detector. The resolution of the measurement is determined by the collimation of the spectrometer and the wavelength spread of the incident beam. The collimation of the beam is defined by the effective source radius  $R_1$  and the radius  $R_2$  of the aperture before the sample, and the distance  $L_1$  between them. The resolution at a particular magnitude of scattering vector is given by

$$\sigma_Q^2 = k^2\sigma_\theta^2 + \theta^2\sigma_k^2 = k^2\sigma_\theta^2 + Q^2(\sigma_\lambda^2/\lambda^2). \quad (2)$$

The variance in the scattering angle  $\sigma_\theta^2$  is given by

$$\sigma_\theta^2 = (1/12)[3(R_1/L_1)^2 + 3R_2^2(L_1^{-1} + L_2^{-1})^2 + (\Delta R/L_2)^2], \quad (3)$$

where  $\Delta R$  is the width of the annulus at a radius  $R$  over which the data are circularly averaged. The variance in the wavelength  $\sigma_\lambda^2$  equals  $(1/6)(\Delta\lambda)^2$  for the triangular wavelength distribution ( $\Delta\lambda = \text{FWHM}$ ) produced by the velocity selector. Hence the  $Q$  resolution is given by

$$\sigma_Q = k/(12^{1/2})[3(R_1/L_1)^2 + 3R_2^2(L_1^{-1} + L_2^{-1})^2 + (\Delta R/L_2)^2 + 2(Q/k)^2(\Delta\lambda/\lambda)^2]^{1/2}. \quad (4)$$

The optimization of the count rate on the detector for a given scattering vector value  $Q$  and resolution  $\sigma_Q^2$  (Schmatz *et al.*, 1974; Mildner & Carpenter, 1984) gives the following relationships between ratios of the transverse to the longitudinal distances:

$$\begin{aligned} (R_1/L_1) &= R_2(L_1^{-1} + L_2^{-1}) \\ &= (2/3)^{1/2}(\Delta R/L_2) \\ &= [2/(3^{1/2})](R/L_2)(\Delta\lambda/\lambda). \end{aligned} \quad (5)$$

This means that the effective source and sample radii are proportional to their distances from the detector and define a cone that converges to a point on the detector. This is shown schematically in Fig. 11. The minimum theoretical scattering vector is given by

$$\begin{aligned} Q_{\min} &= (2\pi/\lambda)(R_{\min}/L_2) \\ &= (2\pi/\lambda)[(R_2/L_2) + (R_1 + R_2)/L_1]. \end{aligned} \quad (6)$$

This is also defined by this optimization to be  $Q_{\min} = (4\pi/\lambda)(R_1/L_1) = (4\pi/\lambda)R_2(L_1^{-1} + L_2^{-1})$ . However, in practice the resolution element size of the detector increases the minimum scattering vector to

$$\begin{aligned} Q_{\min} &= (2\pi/\lambda)(R_{\min} + \Delta R)/L_2 \\ &= (2\pi/\lambda)[(R_1 + R_2)/L_1 + (R_2 + \Delta R)/L_2]. \end{aligned} \quad (7)$$

For comparison purposes, the fluence on the sample is proportional to  $(R_1R_2/L_1)^2$  and the count rate measured at the detector position is proportional to  $[(R_1R_2)/(L_1L_2)]^2$ . The best

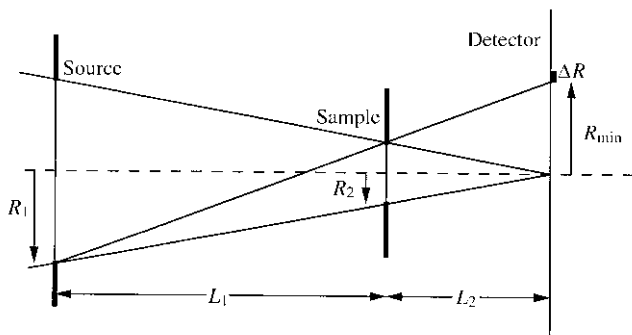


**Figure 11**  
The geometry of the experimental arrangement on a small-angle scattering instrument.

measure of comparison is given by the count rate per useful detector element,  $[(R_1R_2\Delta R)/(L_1L_2)]^2$ , where the element size  $\Delta R$  is given by the larger of the real pixel element sizes or that given by the optimization equation (5). Such a comparison does not penalize the IP technique, with its much smaller pixel sizes than the gas detector.

We thank Jim Bahre of Fuji Medical Systems USA, Inc., for the loan of the gadolinium-loaded IP and its reading equipment. Commercial equipment, instruments or materials are identified in order to specify the experimental procedures in adequate detail. Such identification does not imply recommendation by NIST, nor does it imply that the materials or equipment are necessarily the best for the purpose. This research has been funded by NIST under contact number 50-DKNCB-5-00180.

## References

- Bücherl, T., Rausch, C. & von Seggern, H. (1993). *Nucl. Instrum. Methods A*, **333**, 502–506.
- Cheng, Y. T. & Mildner, D. F. R. (2000). *Nucl. Instrum. Methods A*. In the press.
- Cheng, Y. T., Soodprasert, T. & Hutchinson, J. M. R. (1996). *Appl. Radiat. Isotop.* **47**, 1023–1031.
- Choi, S.-M., Barker, J. G., Glinka, C. J., Cheng, Y. T. & Gammel, P. L. (2000). *J. Appl. Cryst.* **33**, 793–796.
- Cipriani, F., Castagna, J.-C., Lehmann, M. S. & Wilkinson, C. (1995). *Physica B*, **213–214**, 975–977.
- Cipriani, F., Castagna, J.-C., Wilkinson, C., Oleinek, P. & Lehmann, M. S. (1995). *J. Neutron Res.* **4**, 79–85.
- Gilles, R., Keiderling, U. & Wiedenmann, A. (1998). *J. Appl. Cryst.* **31**, 957–959.
- Glinka, C. J., Barker, J. G., Hammouda, B., Krueger, S., Moyers, J. J. & Orts, W. J. (1998). *J. Appl. Cryst.* **31**, 430–445.
- Glinka, C. J., Rowe, J. M. & LaRock, J. G. (1986). *J. Appl. Cryst.* **19**, 427–439.
- Huang, T. C., Toraya, H., Blanton, T. N. & Wu, Y. (1993). *J. Appl. Cryst.* **26**, 180–184.
- Karasawa, Y., Niimura, N., Tanaka, I., Miyahara, J., Takahashi, K., Saito, H., Tsuruno, A. & Matsubayashi, M. (1995). *Physica B*, **213–214**, 978–981.
- Mildner, D. F. R. & Carpenter, J. M. (1984). *J. Appl. Cryst.* **17**, 249–256.
- Né, F., Gazeau, D., Lambard, J., Lesieur, P., Zemb, T. & Gabriel, A. (1993). *J. Appl. Cryst.* **26**, 763–773.
- Niimura, N., Karasawa, Y., Tanaka, I., Miyahara, J., Takahashi, K., Saito, H., Koizumi, S. & Hidaka, M. (1994). *Nucl. Instrum. Methods A*, **349**, 521–525.
- Niimura, N., Minezaki, Y., Nonaka, T., Castagna, J.-C., Cipriani, F., Høghøj, P., Lehmann, M. S. & Wilkinson, C. (1997). *Nature Struct. Biol.* **4**, 909–914.
- Rausch, C., Bücherl, T., Gähler, R., von Seggern, H. & Winnacker, A. (1992). *SPIE Proc.* **1737**, 255–263.
- Schmatz, W., Springer, T., Schelten, J. & Ibel, K. (1974). *J. Appl. Cryst.* **7**, 96–116.
- Takahashi, K., Tazaki, S., Miyahara, J., Karasawa, Y. & Niimura, N. (1996). *Nucl. Instrum. Methods A*, **377**, 119–122.
- Thoms, M., Lehmann, M. S. & Wilkinson, C. (1997). *Nucl. Instrum. Methods A*, **384**, 457–462.
- Wilkinson, C., Gabriel, A., Lehmann, M. S., Zemb, T. & Né, F. (1992). *SPIE Proc.* **1737**, 255–263.